

Electronic Supplementary Information

Thermally Rearranged Polymer Membranes for Desalination

Ji Hoon Kim¹, Sang Hyun Park¹, Moon Joo Lee²,
Sang Min Lee¹, Won Hyo Lee¹, Kang Hyuck Lee¹,
Na Rae Kang¹, Hye Jin Jo¹, Jeong F. Kim¹,
Enrico Drioli^{1, 3, *} and Young Moo Lee^{1, 2, *}

¹ Department of Energy Engineering, College of Engineering,
Hanyang University, Seoul 133-791, Republic of Korea

² Division of Chemical Engineering, College of Engineering, Hanyang University,
Seoul 133-791, Republic of Korea

³ Institute on Membrane Technology (ITM-CNR), University of Calabria, Rende,
Cosenza, Italy

***Corresponding authors:**

Y. M. Lee (ymlee@hanyang.ac.kr),

E. Drioli (e.drioli@itm.cnr.it)

0. Background

Most of the developed MD membranes can be fabricated using two types of fabrication methods: phase inversion method and electrospinning method. The phase inversion method is a well-known conventional technique to fabricate asymmetric membranes with variety of morphologies. On the other hand, the electrospinning method can fabricate highly porous, thin and flexible membrane with high porosity.¹ We have summarized the pros & cons of the two fabrication methods for membrane distillation application as shown in **Table S1**.

Table S1 Summary of pros & cons between phase-separation and electrospun membranes for membrane distillation application.

Membrane Distillation Application	Phase-separation Membrane	Electrospun Membrane
Pros	<i>Stable performance</i> <ul style="list-style-type: none">• High LEP• Narrow pore size distribution	<i>High water flux</i> <ul style="list-style-type: none">• High porosity• Inter-connected pore structure• Large pore size• Thin, rough surface
	Cons	<i>High mass transport resistance</i> <ul style="list-style-type: none">• Thick• Low porosity• Small pore size

As shown in **Table S1**, there is a trade-off between the long-term stability and the MD flux. For instance, membranes fabricated using the phase inversion method shows high stability but relatively lower permeability, and membranes fabricated using the electrospinning method shows high permeability but lower long-term stability.

Table S2 summarizes the recent DCMD publication data in the literature. It can be seen that the membranes prepared using the phase inversion method generally shows lower permeability but excellent long-term stability due to their low porosity and high thickness. Notably, one of the reported data showed stability up to 300 hr.² On the other hand, many researchers have recently focused on preparing electrospun membranes due to their high water flux and excellent salt rejection. However, not many researchers have reported the long-term stability data.

Table S2 Recently published DCMD data of flat-sheet type membranes in literature.

Material	Type	LEP (bar)	Pore size (μm)	Thickness (μm)	Porosity (%)	Feed (°C)	Permeate (°C)	Water flux (Kg m ⁻² hr ⁻¹)	Long-term Stability (hr)	Published year	Ref.
PVDF	Phase separation	2.0	0.12	N/A	N/A	3.5 wt% NaCl _{aq} (80)	DI water (17)	14	48	2014	3
PIFE	Millipore commercial	1.5	0.22	175	70	3.5 wt% NaCl _{aq} (80)	DI water (20)	40	70	2014	4
PVDF / fabric	Phase-separation	6	0.22	213	55	3.5 wt% NaCl _{aq} (50)	DI water (20)	13	240	2012	5
PVDF	Phase-separation	8.9	0.33	330	64	3.5 wt% NaCl _{aq} (50)	DI water (17.5)	15	300	2014	2
TRPBOI TR-NCM-2	Electro-spinning	1.0	0.28	60	83	0.5 M NaCl_{aq} (70)	DI water (17.5)	79	186 (66 + 120)	2015	In this study
SiO ₂ nps PVDF	Electro-spinning	1.8	0.68	130	83	3.5 wt% NaCl _{aq} (60)	DI water (20)	18.9	50	2014	6
PS	Electro-spinning	0.8	0.62	120	78	3.5 wt% NaCl _{aq} (70)	DI water (20)	51	10	2014	7
Ag nps PVDF	Electro-spinning	1.5	0.34	47	66	3.5 wt% NaCl _{aq} (60)	DI water (20)	32	8	2013	8
F-PT	Electro-spinning	0.9	2.7	N/A	N/A	3.5 wt% NaCl _{aq} (70)	DI water (20)	61	N/A	2012	9

As can be seen in **Table S2**, the present TR-PBOI membranes exhibited the highest water flux and excellent salt rejection for a long time compared with other reported electrospun membranes. Most of the electrospun membranes reported in

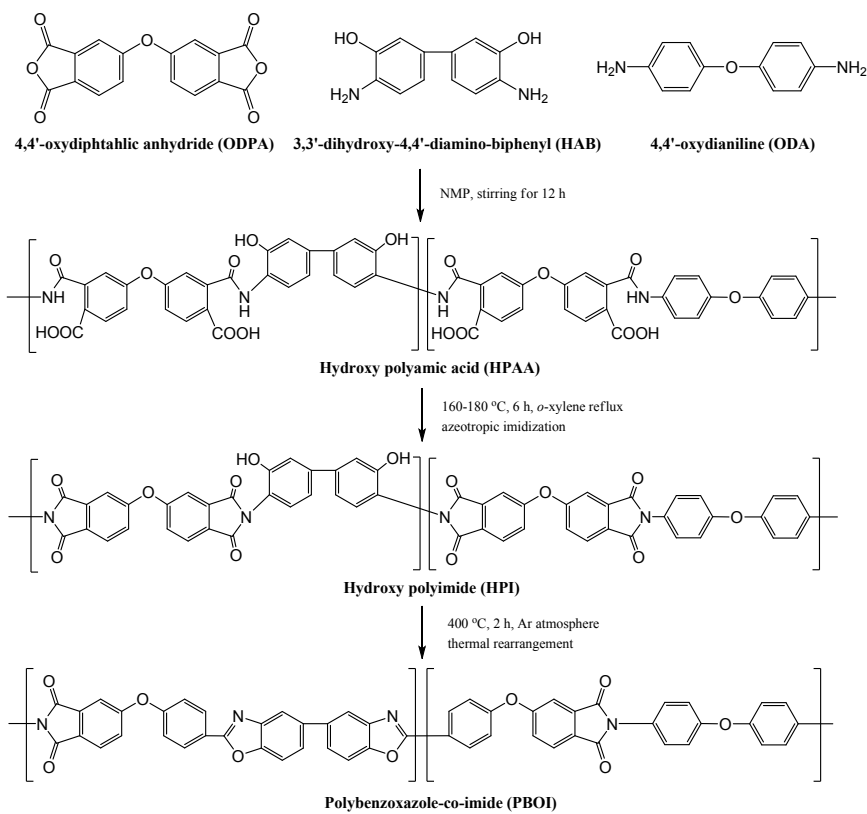
the literature showed significant performance degradation with operation time or did not report any long-term data.

1. Materials

Two kinds of diamines and dianhydride were used for the synthesis of hydroxy polyimide (HPI) as a precursor of thermally rearranged polybenzoxazole-co-imide (TR-PBOI) (**Scheme S1**). 4,4'-oxydiphthalic anhydride (ODPA) was purchased from Shanghai Resin factory Co. Ltd. (Shanghai, China). 3,3'-dihydroxy-4,4'-diamino-biphenyl (HAB) and 4,4'-oxydianiline (ODA) were obtained from Sigma-Aldrich Chemical Co. (Milwaukee, WI, USA). *N*-Methyl-2-pyrrolidone (NMP) and *o*-xylene from Sigma-Aldrich Chemical Co. were used as solvents for the synthesis of polymers, and *N,N*-dimethylacetamide (DMAc), poly(vinyl alcohol) (PVA, Mw of 85,000) and poly(vinyl pyrrolidone) (PVP, Mw of 40,000) were purchased from Sigma-Aldrich Chemical Co. for preparation of nano-fibers and particles.

2. Synthesis of hydroxyl polyimide as a precursor polymer for thermally rearranged polybenzoxazole-co-imide

The procedure for synthesizing hydroxy polyimide is described in **Scheme S1** and in our previous studies.^{3, 4} All monomers (ODPA, HAB, and ODA) were dried overnight in a vacuum oven at ambient temperature. Diamines (ODA and HAB, 25 mmol, respectively) were dissolved in a 500 mL four neck round-bottomed flask filled with anhydrous NMP (80 mL) under a nitrogen atmosphere. Once all diamine powders were completely dissolved, the flask was cooled to 0 °C and ODPA monomer (50 mmol) dissolved in NMP (50 mL) was added to initiate polymerization *via* a spontaneous ring opening reaction with diamines. The solution was stirred overnight and a viscous yellowish hydroxyl polyamic acid (HPAA) solution was obtained. To convert HPPA to hydroxy polyimide (HPI) *via* azeotropic imidization, *o*-xylene (60 ml) as an azeotropic agent was poured into the HPAA solution and the flask temperature was maintained between 160 and 180 °C for 6 hr. After removing the water generated by the imidization reaction, the solutions were precipitated in a water/methanol solution (3:1 ratio) using a mechanical mixer, and they were subsequently dried in a vacuum oven at 150 °C for 12 hr.



Scheme S1 Synthetic scheme for thermally rearranged polybenzoxazole-co-imide.

3. Electrospinning of HPI polymer

A HPI dope solution was prepared by dissolving the polymer (10 wt%) in dimethyl acetamide (DMAc). The HPI solution was stirred overnight at 60 °C and filtered through an 11 µm nylon filter (Millipore, USA) to prepare a homogenous solution. A multi-nozzle electrospinning apparatus (M-tek, Korea) was purchased, and it consisted of 16 needles (23 gauges) and a drum type collector (total area: 0.0021 m²). An HPI solution (40 ml) was electrospun onto a collector covered with PET nonwoven fabric with a 15 cm of tip-to-collector distance using a syringe pump (LB-200, Longer Pump, China) set at a flow rate of 4.0 ml h⁻¹. The voltages at the needles and the collector were 28 kV and -4 kV, respectively. During the electrospinning, the needle set traversed along the x-axis rail (25 cm) at 10 mm min⁻¹ and the collector rotated at 8 rpm to obtain a uniform HPI nanofibrous membrane. After electrospinning, the HPI membrane was dried at ambient conditions overnight to remove residual solvent. Then, the HPI membrane was carefully detached from the PET nonwoven support, and thermal rearrangement was conducted as described in **Section S6**.

4. Preparation of HPI nanoparticles

HPI particles were prepared by reprecipitation method which is one of the particle formation method using a polymer solution, non-solvent and stabilizer. In this study, initially four different kinds of HPI particles were prepared to investigate effect of two different stabilizers (PVP, Mw 55K and PVA, Mw 90K) on the particle morphology using water as the nonsolvent, as summarized in **Fig. S1** below. HPI polymer was dissolved in NMP with 2 wt% of concentration without any stabilizer, and with 2 wt% PVP or 2 wt% PVA, and 5 wt% of concentration with 5 wt% PVP. The solutions are designated like HPI2, HPI2PVP2, HPI2PVA2 and HPI5PVP5. All HPI solutions stirred and filtered using 0.5 μm PTFE syringe filter to obtain the homogeneous solutions without impurities. The polymer solution was mechanically stirred with 300 rpm at 70 °C. Non-solvent added into the polymer solution with 0.05 ml min⁻¹ of adding speed using syringe pump. After preparation of HPI particles, the polymer solution was quenched in an ice bath to prevent aggregation of the particles. The particles were filtered and centrifuged to wash off the residual solvent and non-solvent. After freeze drying at 0 °C for 30 hr or more, the particles were ready to fabricate composite membrane.

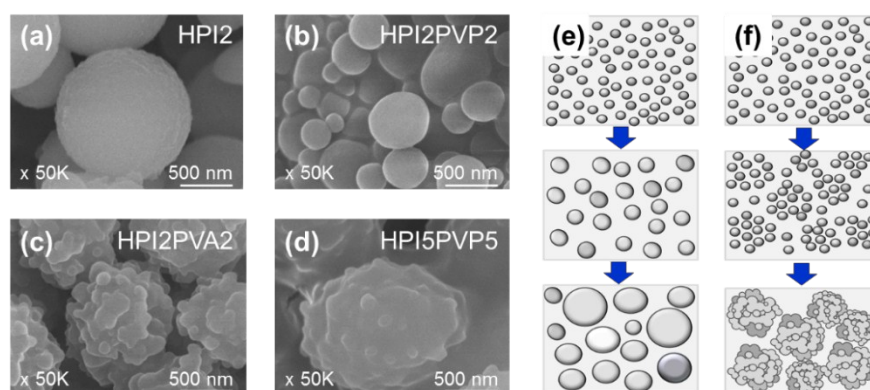


Fig. S1 SEM images of HPI particles in accordance with different stabilizers; (a) without stabilizer, (b) 2 wt% of PVP, (c) 2 wt% of PVA and (d) 5 wt% of PVP. Schematics of suggested particle formation mechanism for (e) spherical and (f) sea-squirt shaped particles.

As shown in **Fig. S1a**, the 2 wt% HPI (HPI2) particles which were fabricated without any stabilizer exhibited crumpled morphology without forming discrete particles. The crumpled morphology was formed due to the particle agglomeration in order to minimize the surface energy. Such agglomeration can be prevented using a surfactant stabilizer such as PVP or PVA.⁵ It can be seen in **Fig. S1b** that 2 wt% PVP additive (PVP2) induced discrete spherical particles with the average diameter of 550 nm. On the other hand, when 2 wt% PVA (PVA2) was used as an additive, the resulting particles exhibited the rough sea-squirt shaped morphology as shown in **Fig. S1c**. Also, the image shows that each particle is made up of many tiny particles fused together. Interestingly, the particles were also porous when examined with TEM (**Fig. 2d1**). Such difference in particle morphology between two additives can be explained using the concept of critical aggregation concentration (CAC), defined as the threshold surfactant concentration at which the interaction between the surfactant and the polymer occurs.⁵ **Fig. S1e and S1f** illustrate the particle formation mechanisms for two different additives. Comparing two additives, 2 wt% PVP was below the CAC and hence each particle grew in size independently (**Fig. S1e**). On the other hand, 2 wt% PVA was above the CAC and hence each particle did not grow in size but formed a secondary particle composed of many primary small particles (**Fig. S1f**). As noted by *Wu et al.* the surfactant acts not only as the stabilizer, but also as the bridge to facilitate agglomeration of primary particles.⁶ As shown in **Fig. 2c1 and 2d1**, the porosity of the sea-squirt shaped particles is induced from the boundaries between the small particles. Notably, it can be seen in **Fig. S1d** that the same sea-squirt morphology can also be induced using PVP

simply by increasing the PVP concentration above the CAC.

5. Fabrication of HPI nanocomposite membranes

HPI particles were dispersed into ethanol at a concentration of 1 wt%. The solution was sprayed onto the surface of the HPI electrospun membrane using a spray gun (HP-TR 2, Iwata, Japan) with N₂ gas at 0.2 kgf cm⁻². The thickness of the coating layer was observed using SEM and the correlation between the coating thickness and the sprayed volume of HPI particles is shown in **Fig. S2**.

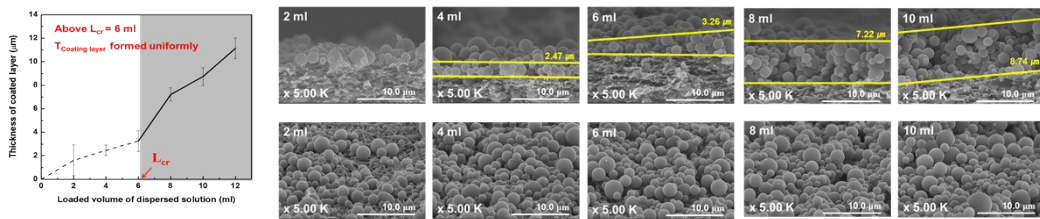


Fig. S2 Thickness of the particle coating layer in accordance with the sprayed volume of the solution with dispersed HPI particles.

The coating layer of HPI particles was uniform and had no defects when > 6 ml solution was sprayed onto the surface. Therefore, we defined a value L_{cr} , which indicates the critical loading amount of a HPI nanoparticle solution for a uniform coating layer and sprayed 8 ml of the solution onto a 0.0088 m² area of the HPI nanofibrous membranes. After spray coating, the HPI composite membrane was dried overnight at ambient conditions to remove ethanol.

6. Thermal rearrangement of HPI membranes

The HPI nanofibrous and nanocomposite membranes were converted to TR-PBOI membranes *via* thermal rearrangement in a furnace at 400 °C under an Ar atmosphere. The furnace was first heated to 300 °C at 10 °C min⁻¹ and equilibrated at 300 °C for 1 hr to remove residual solvent and confirm the azeotropic imidization. Then, the furnace was further heated to 400 °C at 10 °C min⁻¹ and equilibrated for 2 hr for thermal rearrangement.

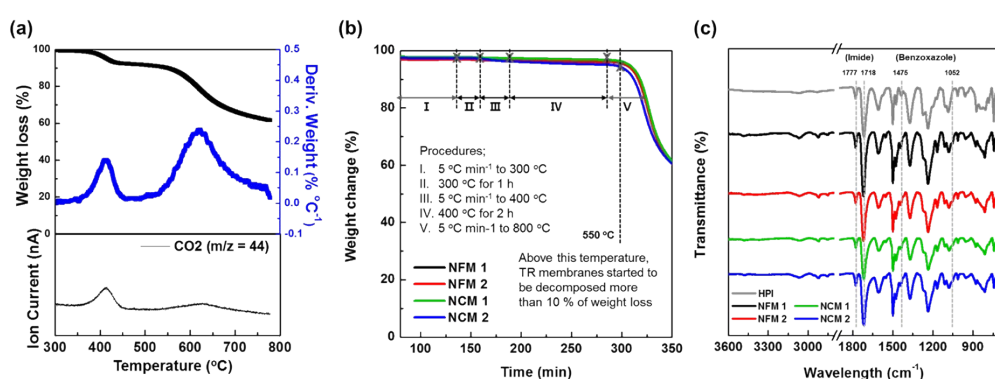


Fig. S3 (a) Thermogravimetric analysis (TGA) and differential thermogram (DTG) curves of HPI nanofibrous membrane with mass spectroscopy of CO₂ on the bottom of the TGA curve. (b) TGA curves and (c) attenuated transmittance reflection infrared (ATR-IR) spectroscopy analysis of TR-PBOI membranes compared with HPI precursor to confirm the thermal stability and thermal rearrangement.

To confirm the thermal rearrangement of the TR-PBOI membranes, thermogravimetric analysis – mass spectroscopy (TGA-mass) and attenuated total reflectance-infrared (ATR-IR) analysis were used for HPI and TR-PBOI membranes. TGA-mass (TA Q-50, TA Instruments, USA and ThermoStar™ GSD 301T, Pfeiffer Vacuum GmbH, Germany) was employed to obtain 100 % TR conversion of the HPI nanofibrous membrane and also to investigate the thermal stability of the TR-PBOI membranes. The HPI membrane was heated up to 800 °C at 10 °C min⁻¹ in a TGA furnace under a nitrogen atmosphere to observe the weight loss of the

membrane during thermal rearrangement. As shown in **Fig. S3a**, the TGA curve of the HPI membrane showed a weight loss and a CO₂ emission peak in the mass spectroscopy data around 400 °C. The curve of the differential thermogram (DTG) also exhibited that the thermal rearrangement rate was the highest at 400 °C. To confirm the thermal rearrangement of all TR-PBOI membranes, each membrane was heated up to 300 °C at 10 °C min⁻¹ and was equilibrated for 1 hr. After that, the membrane was continuously heated to 400 °C at 10 °C min⁻¹ and was equilibrated for 2 hr before finally being heated up to 800 °C at 10 °C min⁻¹ using the TGA. In **Fig. S3b**, All TR-PBOI membranes exhibited excellent thermal stability below 550 °C without significant weight loss, which suggests that the HPI membranes were completely converted to TR-PBOI membranes. In **Fig. S3c**, the evidence of the conversion from HPI to TR-PBOI can also be observed at 1052 and 1475 cm⁻¹, corresponding to the benzoxazole band, using ATR-IR (Nicolet 6700, Thermo Scientific, MA, USA).

7. Characterization

The surface morphologies of the TR-PBOI membranes were verified with field emission scanning electron microscopy (FE-SEM, Hitachi S-4800, Tokyo, Japan), transmission electron microscopy (TEM, JEOL JEM-2000EXII, Tokyo, Japan) and atomic force microscopy consisting of a digital instruments Multimode 8 (Veeco, NY, USA) and diNanoScope V controller (Veeco). Before the characterization, the membranes were dried in a vacuum oven overnight at 70 °C to remove residual solvent. The samples for SEM analysis were coated with platinum for 30 s using platinum sputtering (Hitachi E-1045, Tokyo, Japan) and were observed at 15 kV and 10 mA in the SEM chamber under vacuum conditions. For TEM, the samples were embedded in epoxy resin and microtomed using a RMC MTX Ultra microtome (RMC Products, Tucson, AZ, USA). The TEM images were obtained at accelerating voltages of 120 kV. The membranes were also investigated using AFM tapping mode with a silicon probe (Nanosensors, Switzerland) with a force constant of 1.2 – 20 N m⁻¹. The surface roughness was measured using the Nanoscope 8.10 program, and each sample was measured at three different surface regions. The morphologies of TR-PBOI membranes were summarized in **Fig. 2**, and the morphologies of GVHP as a reference membrane (a porous PVDF membrane purchased from Millipore, USA) are summarized in **Fig. S4** together with the cross section SEM images of HPI and TR-PBOI membranes. The hydrophobicity of the membranes were measured using a contact angle analyzer (Phoenix 300, S.E.O, Ansong, Korea) by placing a droplet of deionized water on the membranes and comparing pictures taken 0.5 s after the droplet had fallen. The contact angles of TR-PBOI membranes are displayed in **Fig. 2** and that of the GVHP membrane is provided in **Fig. S4d**.

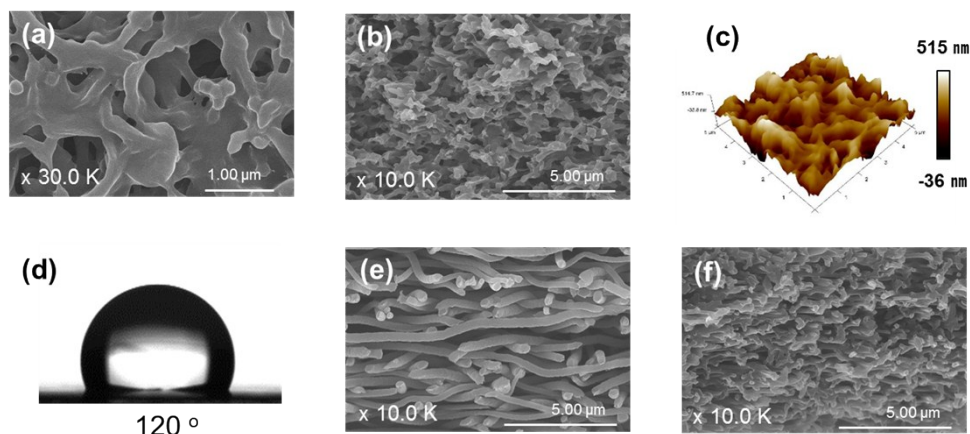


Fig. S4 SEM images of (a) surface and (b) cross section, (c) AFM and (d) contact angle of GVHP membranes. The cross-section SEM images of (e) HPI-NFM-1 and (f) TR-NFM-1.

The mean pore size and pore size distribution of all membranes were investigated using a capillary flow porometer (CFP, 1500AE, Porous Materials, USA) as shown in **Fig. S5**. The samples were immersed in a Galwick solution (surface tension: $15.9 \text{ dyne cm}^{-1}$) for 10 min and were measured using the wet up / dry up method from 0 to 400 psia using N_2 gas.

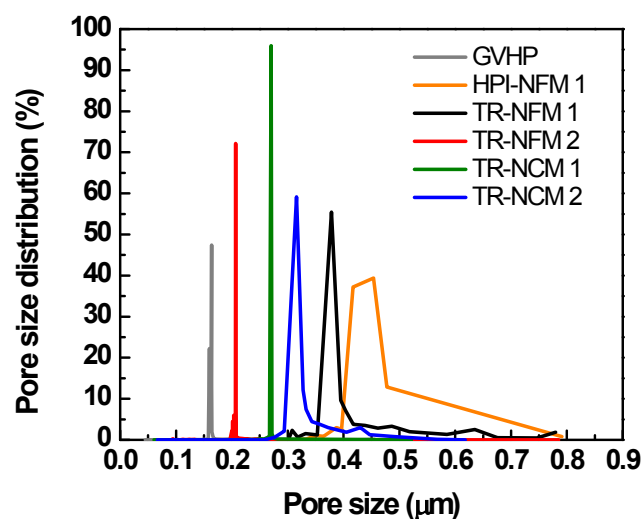


Fig. S5 The pore size distribution of GVHP, HPI-NFM-1, TR-NFM-1, TR-NFM-2, TR-NCM-1 and TR-NCM-2.

The porosity of the membranes was evaluated using n-hexadecane (Alfa Aesar, MA, USA). The samples were prepared at least 5 times for each membrane and the dried and soaked weights of the membranes were recorded. Excess solvent on the surface of the membranes was wiped off before measuring the weight of the soaked membrane. The porosity was calculated using the following equation (S1);

$$porosity (\varepsilon) = \frac{(w_1 - w_0)}{\rho_s} / V_0 \times 100 \quad (\text{S1})$$

where w_1 and w_0 are the weights of polymer membranes dried and soaked in n-hexadecane, respectively, ρ is the density of n-hexadecane, and V_0 means the total volume consisting of the polymer and pores occupied by n-hexadecane.

Thermal diffusivity measurements (NETZSCH, LFA 447 NanoFlash) were conducted using an InSb sensor at 25 °C using a dense membrane in a through-plane direction following ASTM E1461. The thermal conductivity of the membranes was calculated using the following equation (S2);

$$k_m = k_a \times \varepsilon + k_p \times (1 - \varepsilon) \quad (\text{S2})$$

where k_m , k_p and k_a are the thermal conductivities of membrane, polymer and the

8. DCMD test

The test apparatus for direct contact membrane distillation (DCMD) was purchased from Phillos Company (Korea). All DCMD tests were conducted using the Teflon cell, which has a 0.00181 m^2 active area (see **Fig. S6**).

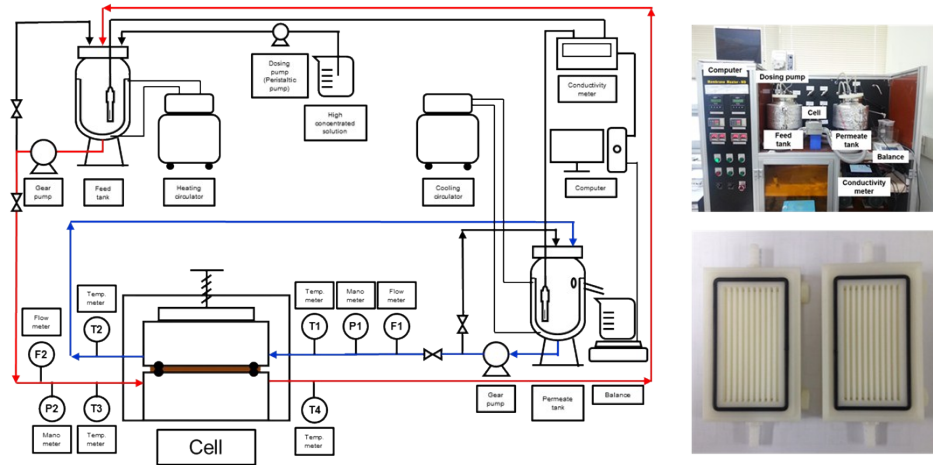


Fig. S6 DCMD apparatus and Teflon cell.

The feed temperature was controlled from 50 to 70 °C and was measured at the inlet and outlet of the cell. The permeate temperature was also checked at the inlet and outlet of the cell, and the average permeate temperature was fixed at 20 °C. All test were operated using a countercurrent flow type consisting of a hot feed and cold permeate flows through the bottom and top parts of the cell, respectively. During the test, the over-flow water from the permeate tank was collected on the beaker and the weight was recorded every 10 min. The conductivities of the feed and permeate tanks were also measured and sent to a computer every 10 min to calculate the salt rejection of the membrane. A dosing pump was employed to maintain the conductivity of the feed tank depending on the water flux of the membrane. The flow rates of feed and permeate were operated in a range of 0.5 to 2.0 ml min^{-1} with a 0.5

ml min⁻¹ step size. The water flux and salt rejection of all the membranes were observed at steady state at least 3 hr after changing the operating conditions.

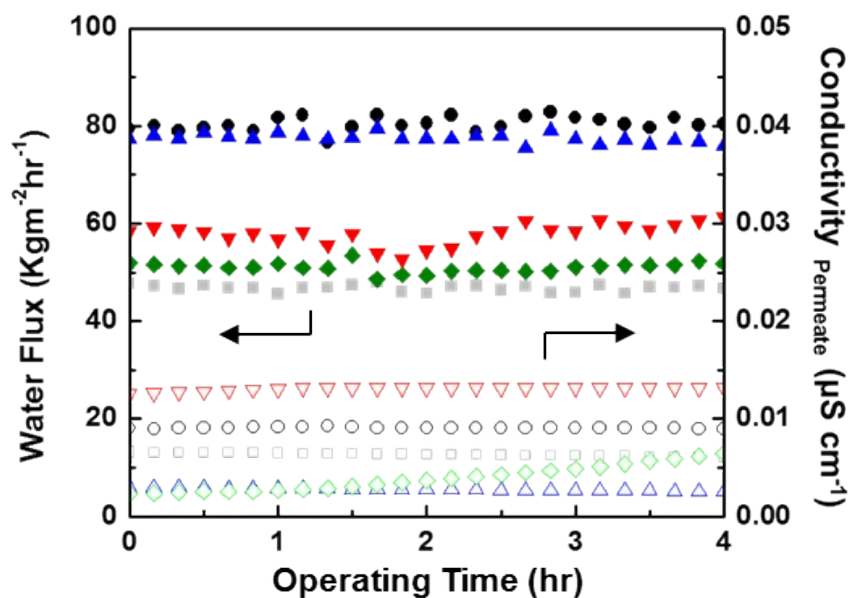


Fig. S7 Water flux and conductivity profiles of GVHP (■), P-PBO (▼), Up-PBO (●), NCM 1 (◆) and NCM 2 (▲) membranes for 4 hr using synthetic sea water (0.5 M NaCl aqueous solution) as a feed (70 °C) and D.I. water as a permeate (20 °C) at a flow rate of 2 L min⁻¹.

As shown in **Fig. S7**, all the membranes exhibited stable MD performance in terms of permeate conductivity. Among those, TR-NFM-1 and TR-NCM-2 exhibited high water flux with excellent salt rejection. Therefore, those membrane were used in a long term stability test.

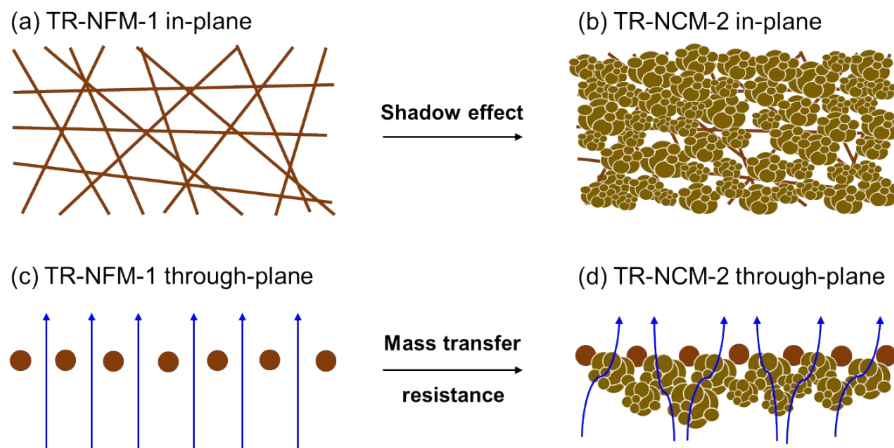


Fig. S8 Illustration of the surface and cross-section of TR-NFM-1 and TR-NCM-2.

Since TR-NCM-2 was coated with porous TR-PBOI particles, the particle coating layer induces a shadow effect to cause the performance difference between the TR-NFM-1 and TR-NCM-2, as shown in **Fig. S8**. As a result, although the particle coating certainly prevents the membrane from wetting, the shadow effect of the particles increased the mass transfer resistance through the coating layer lowering the membrane water flux. The shadow effect of the particles was already reported in the literatures,^{7, 8} where the surface pores were blocked by the particles preventing water evaporation.

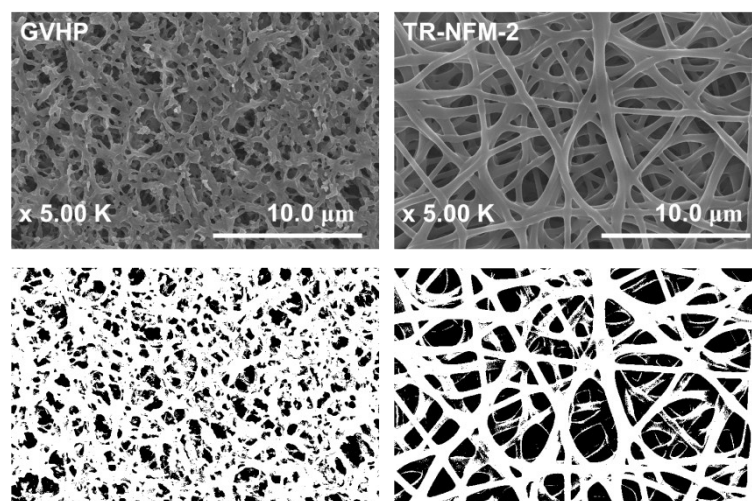


Fig. S9. SEM images and edited SEM images of GVHP and TR-NFM-2 to calculate the

surface porosity. The SEM images were edited by ImageJ program. The surface porosity of GVHP and TR-NFM-2 are 28.7 ± 2.88 and 38.9 ± 2.14 %, respectively.

The porosity (75 %), contact angle (120°) and roughness (146 nm) of GVHP were higher than those (64 %, 100° and 69 nm) of TR-NFM-2. It can be deduced that GVHP membrane would have broader transfer channel for the water vapor, higher water curvature on the surface pores for the water vapor, higher water curvature on the surface pores for the water vapor, and lower temperature polarization (TP) from the induced turbulent flow compared to those of TR-NFM-2. On the other hand, the larger thickness (125 μm) and lower surface porosity (28.7 %, shown in Fig. S9) of GVHP lowered the water vapor transport through the membrane and reduced the effective area for the water vapor to evaporate than those (60 μm and 38.9 %) of TR-NFM-2, respectively (Fig. S9).

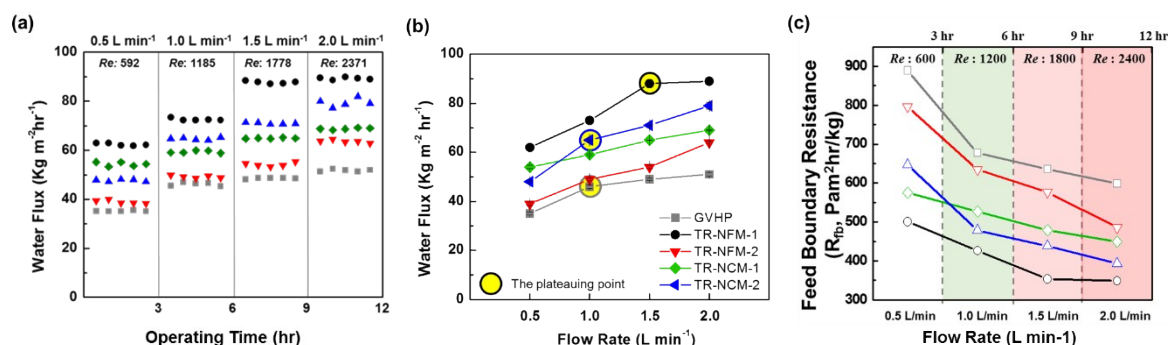


Fig. S10 The water flux (a) and (b), and feed boundary resistance profiles (c) of GVPH (■), TR-NFM-1 (●), TR-NFM-2 (▼), TR-NCM-1 (◆) and TR-NCM-2 (▲) according to different Re (600, 1200, 1800 and 2400) of flow rate.

As shown in Fig. S10, it is well accepted that increasing the crossflow velocity increases the Re number, creating more turbulence on the membrane surface which reduces the temperature polarization, improving the observed flux. Generally, the higher the surface roughness, the higher the turbulence effect. Importantly, the flux improvement with the

increasing Re number typically plateaus off in the form of logarithmic function.⁹⁻¹¹ Hence, the change in flux with change in Re ($\frac{dJ}{dRe}$) becomes lower with higher Re . There is a larger flux improvement when the crossflow velocity increased from 0.5 to 1.0 L min⁻¹ compared to the flux improvement from 1.5 to 2 L min⁻¹, due to the aforementioned logarithmic trend. As can be seen in **Fig. S10c**, the flux values of TR-NFM-2 (red) and TR-NCM-1 (green) increases proportionally to flow rate (Re). On the other hand, the flux data for TR-NFM-1 (black), TR-NCM-2 (blue) and GVHP (gray) exhibited clear plateaueing points, with TR-NFM-1 showing the plateaueing point at higher flow rate. In the tested range of flow rates, TR-NFM-2 and TR-NCM-1 did not show visible plateaueing points. Such trend, of course, is a function many factors including the surface morphology of the membranes.

For instance, the surface roughness values of TR-NCM-2 (133 nm) and GVHP (146 nm) were higher than that of TR-NFM-1 (101 nm). Therefore, the plateaueing points of TR-NCM-2 and GVHP were lower than that of TR-NFM-1. On the other hand, TR-NFM-2 and TR-NCM-1 did not show a plateaueing point in the tested range. Since TR-NFM-2 has low surface roughness (69 nm) and high thermal conductivity (0.122 W m⁻² K⁻¹), we suspect the plateaueing point for TR-NFM-2 would exist at a flow rate higher than 2.0 L min⁻¹. On the other hand, TR-NCM-1 had high surface roughness, the low thermal conductivity with small and narrow surface pore size distribution, and we suspect lower plateaueing point at a flowrate lower than 0.5 L min⁻¹.

The water flux difference was also hopefully explained by the feed boundary resistance (R_{fb}) which represents effect of flow rate on temperature polarization phenomena at feed was derived using following equations:^{12, 13}

$$R_{fb} = \frac{P_f - P_{fm}}{J_w} \quad (\text{S3})$$

where P_f is the vapor pressure at bulk feed, P_{fm} is the vapor pressure at feed membrane surface and J_w is the water flux.

Because the R_{fb} was calculated with considerations of fluid dynamics and heat transfer models at feed, consequently, the R_{fb} could represent the relative effects of temperature polarization at feed as well as the membrane properties for the MD performance. Therefore, the R_{fb} would be adequately explain the difference of observed water flux with a collectively insight of the cell design, fluid dynamics, heat transfer and surface morphologies of the membranes.

The vapor pressure was calculated by Antoine equation:^{12, 13}

$$P_i = \exp\left(23.238 - \frac{3841}{T_i - 45}\right), (i = f, fm) \quad (\text{S4})$$

where T_f and T_{fm} are the temperature at bulk feed and feed membrane surface, respectively.

The T_{fm} can be derived from the energy balance at steady state.^{12, 13}

$$Q = Q_f = Q_m = Q_p \quad (\text{S5})$$

$$= h_f(T_f - T_{fm}) = h_m(T_{fm} - T_{pm}) = h_p(T_{pm} - T_p) \quad (\text{S6})$$

$$T_{fm} = T_f - \frac{(T_f - T_p) \frac{1}{h_f}}{\frac{1}{h_m} + \frac{1}{h_p} + \frac{1}{h_f}} \quad (\text{S7})$$

where Q_i is the heat flux at feed, membrane and permeate at steady state, respectively, and the T_{fm} can be calculated from **eqn (S7)**.

The heat transfer coefficients of membrane, feed and permeate were calculated by followed equations:

$$h_m = \frac{k_m}{\delta} \quad (\text{S8})$$

$$h_i = \frac{Nu_i k_i}{D_h}, (i = f, p) \quad (\text{S9})$$

where the h_m , h_p and h_f are the heat transfer coefficient of membrane, permeate and feed, respectively, the k_m is the thermal conductivity of the membrane and δ is the membrane thickness, and the D_h is the hydraulic diameter.

$$Nu_i = 0.13 Re^{0.64} Pr^{0.38}, (Re < 2100) \quad (\text{S10})$$

$$Nu_i = 0.23 Re^{0.8} Pr^{0.33}, (Re > 2100) \quad (\text{S11})$$

$$Re = \frac{\rho v D_h}{\mu} \quad (\text{S12})$$

$$Pr = \frac{C_p \mu}{k} \quad (\text{S13})$$

where Nusselt (Nu), Reynolds (Re) and Prandtl (Pr) numbers were used for calculate heat transfer coefficient at feed and permeate, respectively, the ρ is the density of the fluid, the v is the mean velocity of the fluid, the μ is the dynamic viscosity of the fluid, and the k is the thermal conductivity.

The feed boundary resistance decreased with increasing Re number (higher flow rates). It can also be seen that the change in the boundary resistance with increasing Re number is different between the membranes. Generally, the change in the boundary resistance with

respect to the feed flowrate ($\frac{dR_{fb}}{dF}$) became smaller at higher Re . Therefore, there was bigger change in the water flux in the lower range of Re compared with the change in the higher

range of Re . In addition, the change in the boundary resistance ($\frac{dR_{fb}}{dF}$) was different between the membranes, as the membranes exhibit different surface morphologies. In the case of TR-NFM-1, ($\frac{dR_{fb}}{dF}$) only became smaller at higher flow rates, whereas ($\frac{dR_{fb}}{dF}$) for TR-NCM-2 got smaller at lower flow rates. The main difference between the TR-NCM-2 and TR-NFM-1 membranes is the presence of TR particle coating layer. Since the surface pore size, surface porosity and roughness which can all influence the evaporation of water molecules as well as the feed boundary resistance. Therefore, we carefully conclude that the flow rate of feed solution has bigger effect to the water flux of TR-NFM-1 due to the lower feed boundary resistance.

After long-term test, the cross-section of TR-NCMs was observed by SEM. As shown in **Fig. S11**, the TR-PBOI particles and nanofibers were still fused together.

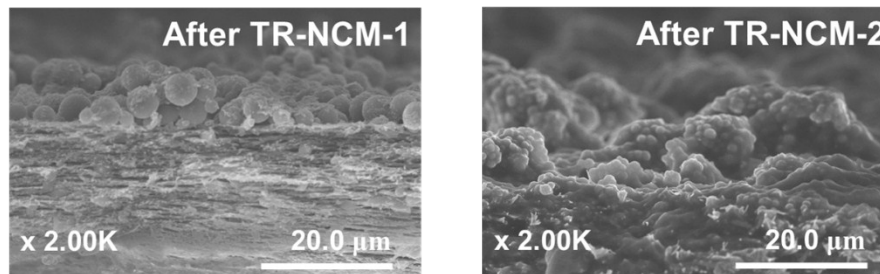


Fig. S11 SEM images of (a) TR-NCM-1 and (b) TR-NCM-2 after long-term test.

The chemical stability test of TR-NFM-1 was conducted in organic solvents, acid and base solution (NMP, DMAc, DMSO, H₂SO₄ and 3 M KOH aqueous solution). As shown in **Fig. S12**, the samples of TR-NFM-1 (2 x 5 cm²) which were immersed in several types of harsh organic solvents, acid and base solution does not dissolve in any solution after three months. After washing out the solvents, any weight change of the membranes was not observed, indicating that the membranes can withstand chemical cleaning conditions.

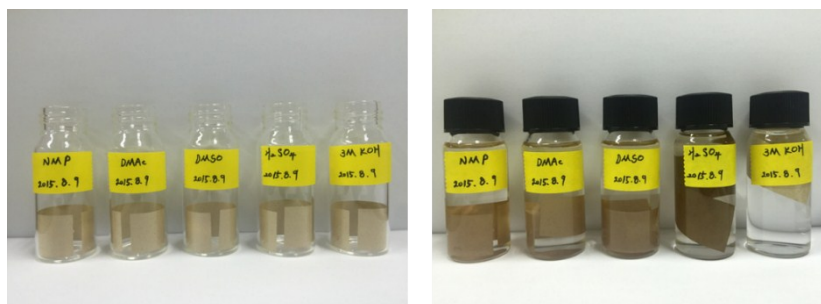


Fig. S12 Chemical stability test in organic solvent, acid and base solutions. (NMP, DMAc, DMSO, concentrated sulfuric acid (H_2SO_4) and 3 M KOH aqueous solution for three months.

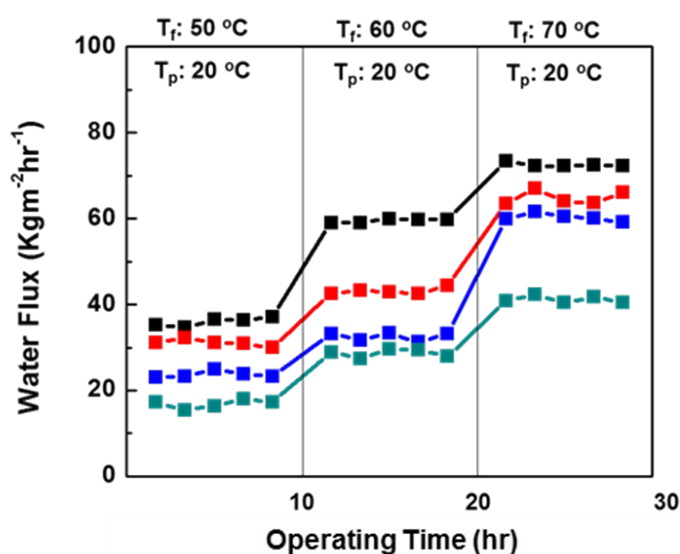


Fig. S13 The water flux profile of TR-NFM-1 was investigated using different feed concentration (0.5 M (■), 1.0 M (■), 3.0 M (■), and 5.0 M (■) of NaCl aqueous solution) with 1 L min^{-1} of flow rates.

9. MCr test

Membrane crystallization (MCr) testing was also conducted using the same apparatus (**Fig. S6**). The feed used was a 352.6 g L^{-1} NaCl aqueous solution at $50\text{ }^\circ\text{C}$. D.I. water was used as a permeate at $20\text{ }^\circ\text{C}$. After pre-heating both feed and permeate solutions, the solutions were circulated in counter current mode with a 1 L min^{-1} flow rate. Then, 5 ml samples were collected at the bottom of the feed tank, and these were observed with an optical microscope (BX51-P, Olympus, Japan). Aliquot samples were sandwiched between slide glasses and

were observed at x20 magnification of the lens (MPlanFL series, Olympus, Japan) using the OM. The surface of the membranes were observed with SEM right after finishing the MCr operation; in order to prepared these samples, an excess solution on the membrane surface was removed and dried in a convection oven at 70 °C overnight. The crystal size and distribution were measured using the imageJ program for more than 100 crystals.

After 3 hr of operation, NaCl crystals $123 \pm 22 \mu\text{m}$ in size, which were produced by TR-NFM-1, were obtained as shown in **Fig. S14**.

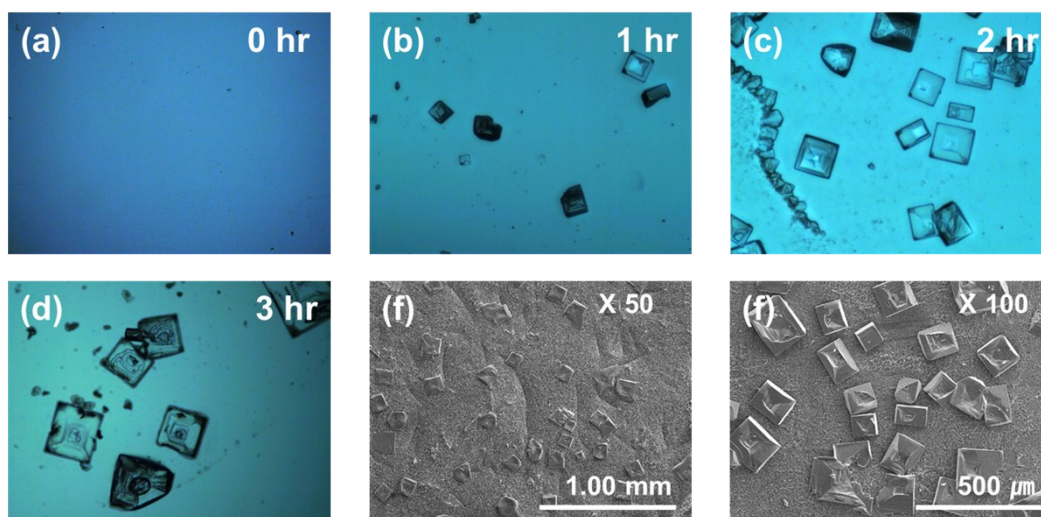


Fig. S14 (a-d) Optical microscopy and (e and f) SEM images of NaCl crystals which were obtained by the MCr test of TR-NFM 1 using a 352.6 g L^{-1} NaCl aqueous solution and D.I. water as feed ($50 \text{ }^\circ\text{C}$) and permeate (20°C) solutions, respectively with flow rates of 1 L min^{-1} .

TR-NFM-1 and TR-NFM-2 were also tested using a 352.6 g ml^{-1} NaCl aqueous solution as feed ($50 \text{ }^\circ\text{C}$) and D.I. water as permeate ($20 \text{ }^\circ\text{C}$) with different flow rates (1 L min^{-1} and 2 L min^{-1}). Aliquots of samples for optical microscopy analysis were obtained at 14 h and at the end of operation. The optical microscopy images were analyzed using the ImageJ program. To estimate the size distribution, at least 100 crystals were measured.

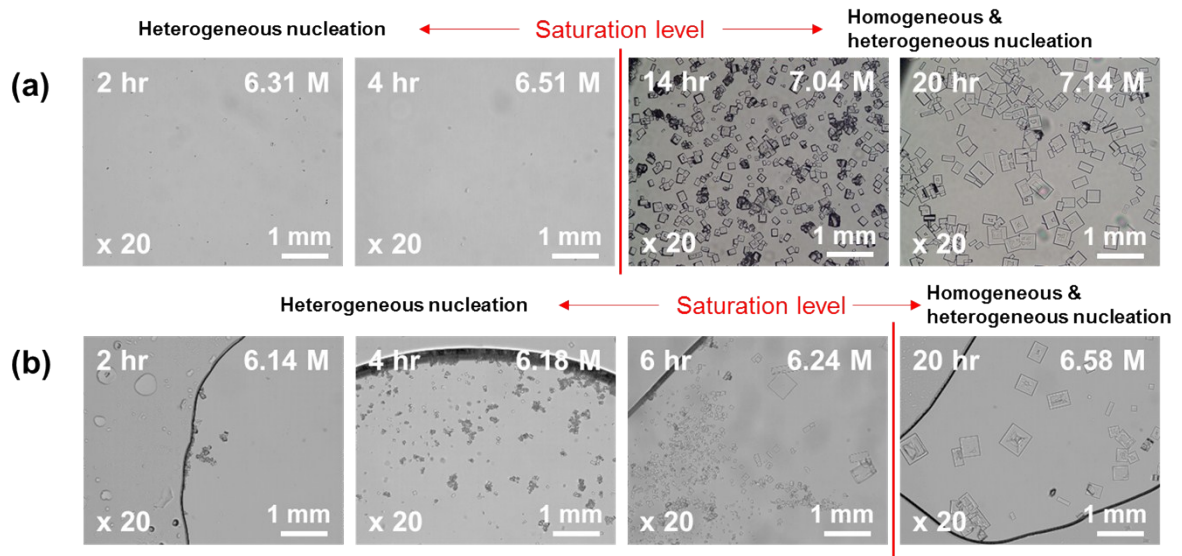


Fig. S15 The optical microscopy images of (a) TR-NFM-1 and (b) TR-NFM-2 according to operation time using 352.6 g L^{-1} NaCl aqueous solution as the feed ($50 \text{ }^{\circ}\text{C}$) and D.I. water as the permeate ($20 \text{ }^{\circ}\text{C}$) with 2 L min^{-1} of flow rate. The saturation concentration of the NaCl aqueous solution was 6.47 M at $50 \text{ }^{\circ}\text{C}$.

To confirm the presence of heterogeneous nucleation, we have conducted further experiment using TR-NFM-1 and TR-NFM-2 membranes as they are most likely to show heterogeneous nucleation. The membranes were tested using 352.6 g L^{-1} of NaCl aqueous solution (near saturation concentration) as the feed ($50 \text{ }^{\circ}\text{C}$) and deionized water as the permeate ($20 \text{ }^{\circ}\text{C}$). Aliquot feed samples were taken and observed using optical microscope at 1 hr interval until the solution reached the saturation level. As shown in **Fig. S15**, in the case of the TR-NFM-2 with $\Delta G_{het}^*/\Delta G_{hom}^*$ value of **0.65**, salt crystals are clearly visible below the saturation level, suggesting they have formed via heterogeneous nucleation. On the other hand, TR-NFM-1 ($\Delta G_{het}^*/\Delta G_{hom}^*$ value of **0.88**) did not show salt crystals until the solution became saturated. Therefore, we believe for stable MD performance, the membrane $\Delta G_{het}^*/\Delta G_{hom}^*$ value should be as close to unity as possible for DCMD process. In addition,

in order to prevent local supersaturation, the membrane should possess high LEP to withstand turbulent feed flow rates.

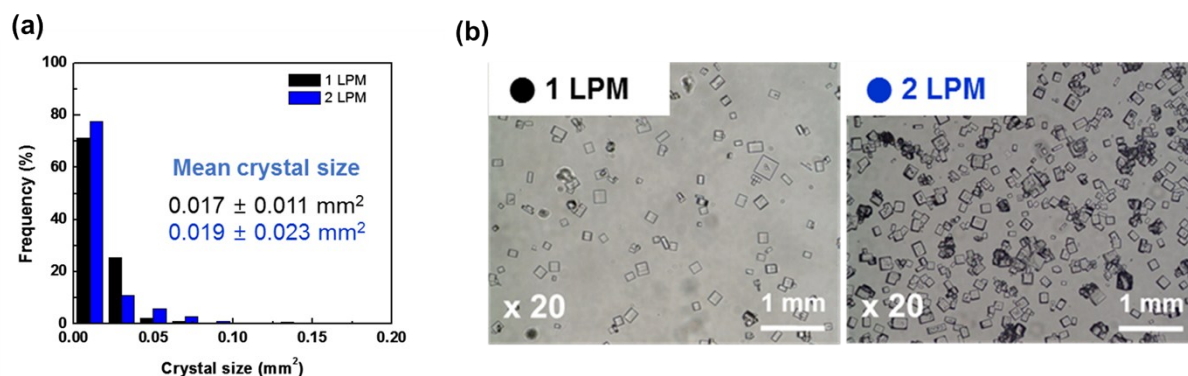


Fig. S16 (a) Crystal size distribution and (b) optical microscopy images of operation at different flow rates: 1 L min⁻¹ (●) and 2 L min⁻¹ (●) after 14 h operation with TR-NFM-1.

TR-NFM-1 was also used to produce Na₂SO₄ crystals using a 184.6 g L⁻¹ Na₂SO₄ aqueous solution (feed, 50 °C) and D.I. water (permeate, 20 °C) as shown in **Fig. S17**. Aliquots of crystallizing solutions for optical microscopy measurement were sampled after 500 and 530 min of operation and were analyzed.

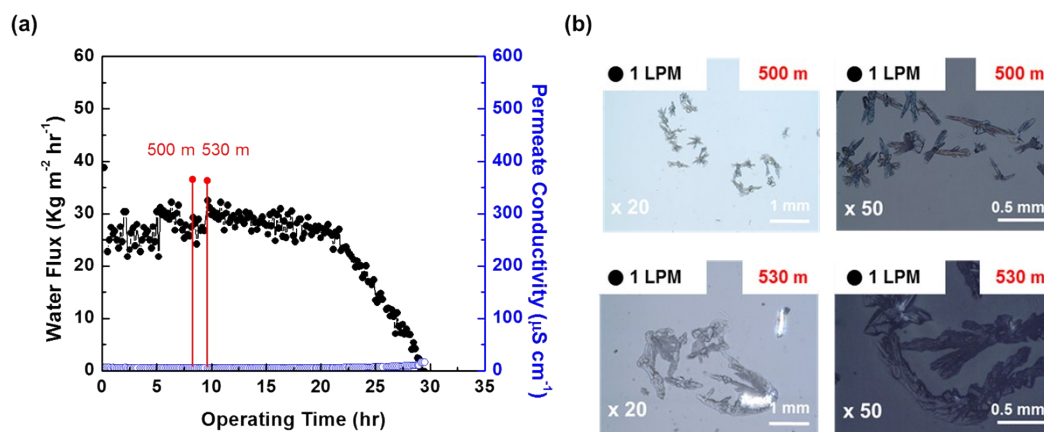


Fig. S17 (a) The water flux and permeate conductivity of TR-NFM-1 were measured with a 184.6 g L⁻¹ Na₂SO₄ aqueous solution as feed (50 °C) and D.I. water as permeate (20 °C) at a flow rate of 1 L min⁻¹. (b) Na₂SO₄ crystals were measured using optical microscopy after 500 and 530 min of MCr operation.

10. References

1. L. D. Tijing, J.-S. Choi, S. Lee, S.-H. Kim and H. K. Shon, *J. Membr. Sci.*, 2014, **453**, 435-462.
2. X. Li, C. Wang, Y. Yang, X. Wang, M. Zhu and B. S. Hsiao, *ACS APPL. Mater. Inter.*, 2014, **6**, 2423-2430.
3. S. H. Han, N. Misdan, S. Kim, C. M. Doherty, A. J. Hill and Y. M. Lee, *Macromolecules*, 2010, **43**, 7657-7667.
4. M. J. Lee, J. H. Kim, H. S. Lim, S. Y. Lee, H. K. Yu, J. H. Kim, J. S. Lee, Y. K. Sun, M. D. Guiver, K. D. Suh and Y. M. Lee, *Chem. Commun.*, 2015, **51**, 3474.
5. A. Pongpeerapat, C. Wanawongthai, Y. Tozuka, K. Moribe and K. Yamamoto, *Int. J. Pharm.*, 2008, **352**, 309-316.
6. J. Y. Xiong, X. Y. Liu, S. B. Chen and T. S. Chung, *J. Phys. Chem. B*, 2005, **109**, 13877-13882.
7. Y. Liao, R. Wang and A. G. Fane, *J. Membr. Sci.*, 2013, **440**, 77-87.
8. Y. Liao, R. Wang and A. G. Fane, *Environ. Sci. Technol.*, 2014, **48**, 6335-6341.
9. F. Laganà, G. Barbieri and E. Drioli, *J. Membr. Sci.*, 2000, **166**, 1-11.
10. T. Y. Cath, V. D. Adams and A. E. Childress, *J. Membr. Sci.*, 2004, **228**, 5-16.
11. A. Razmjou, E. Arifin, G. Dong, J. Mansouri and V. Chen, *J. Membr. Sci.*, 2012, **415-416**, 850-863.
12. S. Srisurichan, R. Jiraratananon and A. Fane, *J. Membr. Sci.*, 2006, **277**, 186-194.
13. J. Phattaranawik, R. Jiraratananon and A. G. Fane, *J. Membr. Sci.*, 2003, **212**, 177-193.